Design of a highly photocatalytically active $ZnO/CuWO_4$ nanocomposite

T. Mavrič[a], M. Valant[a,b], M. Forster[c], A. J. Cowan[c], U. Lavrenčič[d], S. Emin[a,*]

[a] *Materials Research Laboratory, University of Nova Gorica, 5000 Nova Gorica, Slovenia*
[b] *Institute of Fundamental and Frontier Sciences, University of Electronic Science and Technology of China, Chengdu 610054, China.*
[c] *Department of Chemistry, Stephenson Institute for Renewable Energy, The University of Liverpool, UK*
[d] *Laboratory for Environmental Research, University of Nova Gorica, 5000 Nova Gorica, Slovenia*
* Corresponding author. Tel.: 00386 5 365 35 38, *E-mail address*: saim.emin@ung.si (S. Emin)

ABSTRACT

Here we report the synthesis, photocatalytic activity and mechanistic study of a novel charge separation heterostructure (HTS). A $ZnO/CuWO_4$ HTS material is reported for the first time. The nanocomposite (NC) consist of $CuWO_4$ nanoparticles (ca. 200-400 nm) decorated with ZnO nanorods (ca. 30 nm, 100 nm length) and is shown to be a highly active photocatalyst for the decomposition of model contaminants including methyl orange (MO) and terephthalic acid (TPA). The $ZnO/CuWO_4$ interface is shown to be key in controlling the enhanced activity of the composite material. Transient absorption (TA) spectroscopy studies demonstrate that photoinduced charge transfer across the $ZnO/CuWO_4$ interface increases electron-hole lifetimes by 3 orders of magnitude, from < 20 μs in ZnO to 30 ms in the $ZnO/CuWO_4$ NC sample. Our findings show that through interface design efficient HTS materials can be prepared for a wide range of photocatalytic applications.

Keywords: photocatalysis, heterostructure, nanocomposite, methyl orange, terephthalic acid

1. Introduction

Photocatalysis is considered to be a promising green technology, with applications for the production of solar fuels, chemical transformations and remediation of pollutants [1-3]. Research has primarily focused on the use of semiconductor metal oxides, with TiO_2 and ZnO being the most widely studied materials [4,5]. ZnO is a particularly interesting photocatalytic material due to the facile growth of different morphologies, ease in controlling the size of nanoparticles (NPs) and lower material costs [6]. The efficiency of a photocatalytic material can be considered to be the product of a number of individual factors such as the efficiency of; (i) light harvesting, (ii) initial charge separation, (iii) subsequent transport of electrons and holes to the semiconductor/liquid interface and (iv) charge utilisation (catalysis). [7,8] The bandgap of ZnO (3.1 eV) means that *ca.* 4.6% of the energy available in the AM1.5 spectrum can be absorbed. However internal losses due to the recombination of photogenerated electrons and holes in competition with processes (ii)-(iv) severely limit the photocatalytic activity of ZnO and the yield of photogenerated charges that are actually utilised is

often very low. It is therefore important that strategies to retard electron-hole recombination and improve the internal efficiency of ZnO based materials are developed. The formation of two- or multi-component semiconductor heterostructures (HTS) has been explored by numerous works with the aim of delivering new materials with superior electrical, optical, catalytic and mechanical properties [9-13]. Semiconductor-semiconductor HTS are divided into several groups based on the relative position of conduction band (CB) and valence band (VB) edge levels of semiconductor 1 (abbreviated – S1) and semiconductor 2 (abbreviated – S2) [14]. Type-I HTS represents a system where the CB and VB of S2 are enclosed within the CB and VB of S1. A typical example of type-I HTS is ZnO/Bi_2O_3 [15]. Type-II HTS are formed when there is a downward shift of the CB and VB of S2 with respect to S1. Examples include ZnO/TiO_2 [16], ZnO/SnO_2 [17], ZnO/WO_3 [18], ZnO/CdS [19] or ZnO/ZnSe [20]. HTS systems are attractive due to the fact that efficient interface charge transfer between phases enables the formation of long-lived charges, thus hindering the recombinations [21]. However, in many cases direct measurement of the charge carrier lifetime in the HTS is not carried out and instead the activity of a ZnO heterojunction is inferred from the increase in photocatalytic activity for the degradation of organic contaminants [22-26,]. It is therefore apparent that althought significant progress has been made towards improving the internal efficiency of ZnO based photocatalysts, work examining in detail the role of ZnO – semiconductor itnerfaces on charge carrier lifetimes is required. Here we utilise transient absorption (TA) spectroscopy measurements to directly measure the dynamics of photogenerated charges and correlate these to the observed photocatalytic activity for a previously unreported HTS junction, $ZnO/CuWO_4$.

$CuWO_4$ is attracting increasing interest for both photoelectrochemical (PEC) water splitting [27-29] and degradation of organic pollutants [21,30-32]. The band gap of $CuWO_4$ is close to an ideal material (i.e., ~2.2 eV) [33] corresponding to a theoretical solar-to-hydrogen (STH) efficiency of ~13% and $CuWO_4$ also exhibits good stability against photocorrosion at neutral pH [34]. However it has been widely shown that electron-hole recombination in $CuWO_4$ alone is rapid [27-30] with large electrochemical biases being applied to photoelectrodes and relatively low photocatalytic yields being achieved. We however are motivated by the proposed band alignment that will occur at a $ZnO/CuWO_4$ interface. Based on published conduction and valence band edges for both ZnO and $CuWO_4$ [35], we postulated that photoelectron transfer from ZnO to $CuWO_4$ may occur, offering a route to improved charge separation lifetimes. Indeed our TA studies demonstrated that photoinduced charge transfer across the $ZnO/CuWO_4$ interface increases electron-hole lifetimes by 3 orders of magnitude compared with ZnO NPs. The carrier lifetimes recorded in this study are remarkably long for a photocatalyst particles in an inert (argon) atmosphere, exceeding many other HTS systems such as $TiO_2/CdSe$ [36], $WO_3/BiVO_4$ [37], or $TiO_2/CuInS_2$ [38]. This greatly enhanced charge separation lifetime in $ZnO/CuWO_4$ NC directly correlates to an improved photocatalytic activity towards MO and TPA degradation, with the activity of the composite exceeding that of the sum of the individual components.

2. Experimental

2.1. Materials

Ethylene glycol (EG, 99%), polyvinylpyrrolidone (PVP, M.W. 8000), copper (II) acetate monohydrate ($Cu(O_2CCH_3)_2.H_2O$, 98%), sodium tungsten oxide dehydrate ($Na_2WO_4.2H_2O$, 99%), methyl orange (MO, ACS grade) and terephthalic acid (TPA, 98%) were analytical grade and purchased from Alfa Aesar. Zinc acetate dehydrate ($Zn(O_2CCH_3)_2$, 99%) was obtained from Sigma Aldrich. All experiments were carried out using deionized water.

2.2. Synthesis of ZnO and $CuWO_4$ NPs

ZnO and $CuWO_4$ were both hydrothermally synthesized separately. Zinc oxide nanorods were obtained following a synthethic procedure developed by us [39]. A typical synthesis is: 450 mg of $Zn(O_2CCH_3)_2$ dispersed in a EG/d.H_2O mixture with the ratio 30 mL/2 mL. The obtained clear liquid was then transferred into a 100 mL Teflon cup and sealed in a steel autoclave for 3h at 180 °C. After it was cooled to room temperature, the obtained white suspension was washed several times with double deionized water and centrifuged (10 min, 8800 rpm). The obtained ZnO powder (~ 110 mg) was dried in air at 110 °C for 2h.

$CuWO_4$ NPs was synthesized by dissolving 2 g of PVP in 70 mL of deionized water [21]. After the solution became transparent, 1.37 g of $Na_2WO_4.2H_2O$ and 0.83 g of $Cu(O_2CCH_3)_2.H_2O$ were added. The flask was put in an oil bath and heated to 85 °C under vigorous stirring. After 3h the flask was cooled down to room temperature and the obtained $CuWO_4$ NPs were collected by centrifugation (10 min/8800 rpm). Complete cleaning of the NPs from residual organic matter was achieved by repeating the washing and centrifugation steps several times. Drying was done in air at 110 °C for 2h. Crystallization of the obtained $CuWO_4$ powder was achieved by heat treatment at 500 °C in air.

2.3. Preparation of ZnO/$CuWO_4$ composite

Preparation of the ZnO/$CuWO_4$ composite was accomplished by mixing the two types of pre-synthesized powders following ref. [29] for CuO/$CuWO_4$. In a mixture of ethanol and distilled water (3:2 volume ratio) 40 mg of $CuWO_4$ NPs was first dissolved and sonicated for 10 seconds, later 100 mg of ZnO were added and sonicated for 30 min. Then the mixture was sealed and magnetically stirred overnight at room temperature. The next day the powders were collected by centrifugation, washed once in ethanol and dried at 100 °C for 2h. Dynamic light scattering (DLS) experiments were used to measure the NPs sizes (see supplementary data).

2.4. Material Characterization

MiniFlex 600 Benchtop X-ray Defractometer (Rigaku) equipped with Cu-K_α source (1.541 Å) was used to identify the phases. Crystal structure and morphology of NPs were determined by a JEOL 2100F transmission electron microscope (TEM) equipped with an energy dispersive X-ray (EDX) spectrometer (Oxford instrument). Diffuse reflectance spectra were recorded on a Lambda 650S (PerkinElmer) spectrophotometer using Spectralon reflection standard as a reference. The reflectance data were converted to absorbance data using the Kubelka−Munk transformation [40]. TA studies of ZnO and ZnO/$CuWO_4$ samples were done with a 355 nm light source (pulsed laser, 6 ns, Continuum Surelite SL-10). The samples were in the form of thin films deposited on microscope glass slides. The laser was set to *ca.* 250 μJ cm^{-2} per shot with a repetition rate of 0.67 Hz. A 75 W Xe lamp with

a monochromator was used as a probe light source with the light being transmitted through the sample measured by a Si-PIN photodiode once it has been passed through an additional monochromator to remove stray laser light scattered by the sample. The max time resolution of the experiment was ~1 μs and the maximum spectral resolution +/- 4 nm. Prior to the measurements the samples were placed in a furnace (air) for 30 min at 400^{o}C to remove any surface organic contamination and, allowed to cool down to room temperature, and then placed into an Ar purged quartz cuvette. Particle sizes were measured by using dynamic light scattering instrument (Brookhaven) equipped with 35 mW (λ_{ex}=658 nm) solid state laser.

2.5. Photocatalytic tests

The photocatalytic efficiency was tested by monitoring a decay of 1×10^{-5} M solution of MO (pH=5.0) in presence of 50 mg of powdered photocatalysts ($CuWO_4$/ZnO, ZnO, $CuWO_4$, TiO_2 P25) in 100 mL aqueous solution. After introduction of the photocatalyst, the solution was sonicated for 5 seconds, ensuring good dispersibility of the powders. The obtained suspensions were transferred into a Teflon cell with a quartz glass window and kept in dark for 30 min to achieve the adsorption-desorption equilibrium. Irradiation was performed with a 400 W mercury lamp (Photochemical Reactors Ltd., Model 3040) emitting both UV and visible light (see Appendix A). Stability of the irradiation was achieved by turning on the lamp 1 hour prior to the irradiation tests. The distance between the lamp and the cell was fixed to 30 cm. At given time intervals 4 mL aliquots were extracted from the main solution and centrifuged at 8800 rpm for 5 min. UV-vis spectra of the transparent dye solutions were recorded on a Perkin Elmer Lambda 650S spectrophotometer. From the absorption peak at 464 nm, the degradation of MO was evaluated. The photocatalytic activity of the NPs was further tested with 1×10^{-4} M TPA (pH=5.1), using the same experimental procedures as described for MO. The concentration of the TPA was recorded via an HPLC signal (HP 1100 Series chromatograph) on a diode array detector, for 2-hydroxyterephthalic acid (HTPA), as one of the photocatalytic oxidation products, on fluorescence detector. The concentration values were obtained from the integrated area under the absorbance (for TPA) and fluorescence curves (for HTPA).

3. Results and discussion

3.1. Structural and optical characterization

Figure 1a shows the XRD patterns of ZnO, $CuWO_4$ and ZnO/$CuWO_4$ samples. The pattern of ZnO matches with hexagonal ZnO (P63mc, PDF card No. 9004178). The lattice parameters (a = b = 3.246 nm, c = 5.203 nm, α = β =90.000°, γ = 120.000°), calculated with Rietveld refinement, agree with the zincite values from the reference card. Prior to calcination we obtain a relatively amorphous material but following calcination (500°C) a $CuWO_4$ pattern can be indexed according to the triclinic $CuWO_4$ polymorph (P–1, PDF card No. 2101692) with the following calculated lattice parameters: a = 4.708 nm, b = 5.845 nm, c =4.884 nm, α = 88.347°, β = 92.505°, γ = 97.218°. The crystallite size, calculated from diffraction peak broadening ((101) plane ZnO, (001) plane $CuWO_4$) using Scherrer's formula [41], was found to be similar for the both phases, ~40 nm. Furthermore, TEM studies were used to estimate the NPs size and morphology. The TEM image of a typical ZnO/$CuWO_4$ NC particle is presented in Fig. 2a. The big dark oval shaped objects are $CuWO_4$ particles. The size of

these objects is in the range of 200 to 400 nm. The $CuWO_4$ particles are surrounded and covered by smaller ZnO nanorods. The dimensions of the ZnO nanorods are ~30 nm in diameter and ~100 nm in length. The sizes of ZnO NPs can be tuned in different ways such as by changing the reaction temperature, duration of synthesis, concentration of reactants or use of stabilizing agent PVP [39]. For example, as reported earlier the use of PVP leads to the formation of ZnO NPs with shorter length [39]. It's worth mentioning that the ZnO NPs show polydispersity over sizes. The aspect ratio, length divided by width, of the ZnO nanorods is significant low. Because of this reason the (002) peak, sign for preferential growth along the c-axis, is only slightly more intense than the (101) peak. Furthermore, analyses of the XRD data showed that the calculated crystallite sizes of ZnO and $CuWO_4$ obtained from XRD and measured by TEM are different. The discrepancy stems from the fact that the NPs are polycrystalline. The SAED pattern taken from the object in Fig. 2a confirms the polycrystalline nature of this NC (Fig. 2b). STEM image and elemental maps of the NC are presented in Fig.2(c-g). As expected, Zn and O are uniformly distributed throughout the marked area. The location of Cu and W rich regions coincides and is limited to the bigger particles. Energy dispersive X-ray (EDX) spectrum taken from a localized spot confirms that the bigger particles are composed mainly of Cu and W (Fig.2h).

UV-vis diffuse reflectance studies were used to determine optical properties of ZnO, $CuWO_4$ and ZnO/$CuWO_4$ samples (Fig. 3). ZnO, as a wide band gap (~3.1 eV) semiconductor, shows absorption only in the UV region below 400 nm. The absorption spectrum of $CuWO_4$ extends into the visible region, toward longer wavelengths. The broad absorption peak at ~400 nm suggests that several electronic transitions contribute to the observed absorption. It is well documented that $CuWO_4$ exhibits three types of bands in the absorption spectra [42,43]. The first type of band is due to a ligand-to-metal charge transfer (LMCT). The polyatomic WO_4^{2-} anion exhibits O(2p) → W(5d) transition centred at about 400 nm ($CuWO_4$ - 500 °C). The second type is a transfer of electrons from the partially filled d-orbitals of Cu^{2+} to the empty W 5d based molecular orbitals on the tungstate group. This transition is labeled as a metal-to-metal charge transfer (MMCT) and the band appears at longer wavelength than LMCT. The third type involves *d–d* transitions in Cu^{2+} and is positioned above 650 nm. Tauc plots were used to determine band gap energies (E_g) of ZnO and $CuWO_4$. Plotting the photon energy vs. $[F(R)h\nu]^{m/2}$ where m is 1 for indirect and 4 for direct transitions allowed us to identify the type of the transition. In the case of ZnO the spectrum fits to a direct band gap energy (~3.1 eV) which is similar to other reports [44]. As for $CuWO_4$ sample, the data fits well either to a direct (2.3 eV) or an indirect (2.0 eV) transition in a manner similar to literature reports [45-47].

3.2 Determining the role of a ZnO/$CuWO_4$ interface on charge carrier dynamics

The transient absorption (TA) spectrum of ZnO shows no long-lived features (>20 μs) confirming that the majority of recombination of photoinduced charges happens very fast, within 20 μs after UV light excitation, in line with past reports on ZnO charge carrier kinetics in the absence of a chemical scavenger or external bias (Fig. 4a) [48-51]. As no record of $CuWO_4$ TA data could be found in the literature this sample was examined first. No clear (> $2x10^{-5}$ O.D.) transient features were observed on the μs to s timescale following UV excitation (Fig. 4a). On the other hand, the TA spectrum of the ZnO/$CuWO_4$ composite (Fig. 4b) is dominated by a strong band at ~500 nm however the effective

cut-off of this experiment, (450 nm) prevents accurate determination of the band maxima. We also observe a weaker absorption feature at longer wavelengths (> 600 nm) in the TA spectrum of ZnO/$CuWO_4$. Initially, the signal at ~500 nm is bleached, in line with the previously recorded spectrum of electrochemically reduced ZnO (see ref. [49]), with the loss of the ground state signal due to an accumulation of photoelectrons in the conduction band and shallow traps (a Burstein shift). It should be noted that the exact assignment of the ZnO bleach at ~500 nm is still somewhat debated with some reports proposing photoluminescence (PL) or a change in refractive index for the ZnO due to a high concentration of photoelectrons [48], however experiments in the absence of the probe light allow us to rule out the possibility of a PL contribution. Kinetics recorded from the ZnO/$CuWO_4$ NC at 550 nm can be fitted to a minimum of 3 exponential components (Fig. 4c), with the negative signal becoming positive with lifetimes of <1 μs, 15 ± 2 μs and the resultant positive feature decaying at 31 ± 4 ms. We assign the fastest component (which decays at a rate greater than we can accurately measure) to fast electron-hole recombination within the ZnO and from scattered laser light incident on the photodiode. The second component, corresponding to a recovery of the bleach and a growth of a positive signal has a fitted lifetime of 15 μs and this is proposed to be due to electron transfer from the ZnO conduction band (CB) and trap states to $CuWO_4$ as shown in the scheme (Fig. 4d). A long-lived kinetic component corresponds to the slow decay of a positive spectral feature that has the same shape as the previously observed bleach. This is due to holes accumulated in the ZnO, which effectively lowers E_F. The lower trap/CB occupancy enhances the light absorption close to the band edge – essentially the reverse of a Burstein shift. Overall the spectral data supports the assignment of electron transfer from ZnO to $CuWO_4$. We also note that it is thermodynamically feasible that migration of holes from the ZnO VB to the $CuWO_4$ VB may occur, essentially leading to electron-hole recombination. The slow recombination of the long-lived TA signal (31 ± 4 ms) at 550 nm, appears to be due to electron-hole recombination as under argon no charge scavenging by surface species is expected to occur. Therefore, we assign this slow component to either hole transfer to the $CuWO_4$ from ZnO leading to electron-hole recombination on $CuWO_4$, or to direct back electron transfer from the $CuWO_4$ conduction to the ZnO valence band hole. Critically the rate of charge recombination has been decreased by ~ 3 orders of magnitude (from < 20 μs to *ca.* 30 ms) by the presence of the $CuWO_4$/ZnO interface. At this point, we can address the potential accumulation of holes in the valance band of $CuWO_4$. Although $CuWO_4$ in the composite material is able to absorb some of the incoming light, our TA measurements show no evidence of these charges persisting, suggesting sub microsecond internal recombination continues to dominate.

3.4. Photocatalytic activity

As the TA experiments indicate that the HTS junction material has greatly increased charge carrier lifetimes following UV excitation we have examined the photocatalytic activities of ZnO, TiO_2, $CuWO_4$ and ZnO/$CuWO_4$ NPs for the degradation of MO and TPA. Here, TiO_2 was used as a reference UV active photocatalyst. During the 180 min illumination period $CuWO_4$ NPs showed no photoactivity for degradation of MO (Fig. 5). On the other hand, a significant degradation is observed in the presence of ZnO, TiO_2 and ZnO/$CuWO_4$. The highest degradation efficiency of MO was obtained with the ZnO/$CuWO_4$ NC in 60 min. The lack of photoactivity in $CuWO_4$ indicates that this sample contain structural defects (or mid gap states) that lead to fast recombination of the

photogenerated charges [32] in-line with our TA studies. The photocatalytic degradation follows first-order kinetics (Fig. 4b). The degradation rate constant (k) of ZnO/$CuWO_4$ is 0.052 min^{-1}, making it 2 times the k of pure ZnO which is 0.022 min^{-1}. It is useful to keep in mind that nanocrystalline ZnO shows a maximum photoactivity in the pH range of 6≤pH≤11 [52]. It is generally agreed that in acidic environment (pH≤4) dissolution of ZnO NPs can take place according the following equations: $ZnO(s) + H^+ \leftrightarrow Zn^{2+} + H_2O$ or $ZnO(s) + H^+ \leftrightarrow ZnOH^+$ [53]. In the present study the pH of both MO and TPA solutions were in the order of ~5 and if dissolution of ZnO NPs happens it should be at the minimal levels. Indeed, in the past we performed stability tests of ZnO NC and no visible deterioration of photoacatalytic activity has been noticed during 80 min UV-vis irradiation period [39]. A reproducibility test from 3 cycles shows that ZnO/$CuWO_4$ NC slightly loses its activity after the 3-rd run suggesting that there could be some detachment of the ZnO from $CuWO_4$ NPs (Fig. 6). This shortcoming can be overcome by hydrothermal growth of ZnO NPs directly in the suspension of presynthesized $CuWO_4$ NPs to allow better connection between the two types of crystals.

In recent years, terephthalic acid (TPA) has become a model compound for evaluation of photocatalytic activity of semiconductor NPs [54-56]. Several intermediates, aromatic and aliphatic, have been reported to be detected during TPA degradation [31,40,57]. One of the well-known intermediates, 2-hydroxyterephthalic acid (HTPA), is a fluorescent marker due to the fact that its occurrence is proportional to the generated •OH radicals [58,59]. Fig. 7 shows the normalized degradation of TPA and also HTPA concentrations in the presence of ZnO, TiO_2, $CuWO_4$ and ZnO/$CuWO_4$. The photocatalytic experiments were conducted under N_2, O_2 and air. After purging of N_2 gas through the suspensions we noticed that the photocatalysts show photocatalytic activity for degradation of TPA. The aim of this experiment was to reveal the effect of O_2 on the photocatalytic reactions. Under these conditions ZnO NPs are least photoactive. Comparing these data with the amount of HTPA formation we can see that ZnO/$CuWO_4$ NC shows a higher degree of HTPA formation than ZnO and TiO_2. Usually, the formation of HTPA reaches a maximum and later follows a reduction due to further oxidation reactions as observed in early studies [56]. The accumulation of HTPA in ZnO/$CuWO_4$ system indicates that mineralization of HTPA is not so fast and complete. Furthermore, the photocatalytic experiments performed in air and after bubbling of O_2 through the photocatalysts aqueous dispersion give us some hints about the mecahanisms of TPA and HTPA degradations. Under an O_2 rich environment the ZnO/$CuWO_4$ NC shows the highest photoactivity reaching 90% degradation efficiency of TPA. Here the role of O_2 is to capture photoexcited electrons in ZnO/$CuWO_4$ NC and use them to generate superoxide anion radicals ($\bullet O_2^-$). The final step of these species are hydroxyl radicals (•OH) which are the oxidants of organic molecules. Moreover, we also monitored the degradation of HTPA under these aforementioned cases. We found that the fastest way to decompose TPA with a minimum amount of formed HTPA is in O_2 rich (saturated) solutions. The pathways for degradation of TPA and HTPA in the presence of ZnO/$CuWO_4$ NC are given in Fig. 8. The generation of •OH can be achieved either by photogenerated holes or photoexcited electrons (via $\bullet O_2^-$). Under reduced O_2 levels (e.g. N_2 purged) the photo-degradation of TPA is slow. However, under saturated O_2 environment the decomposition is fast as photogenerated •OH can attack both TPA and HTPA.

4. Conclusions

We have prepared a novel ZnO/$CuWO_4$ photocatalyst from presynthesized ZnO and $CuWO_4$ NPs with the aim of utilising a semiconductor-semiconductor (S-S) junction to retard electron-hole recombination losses. The use of SS junctions to enhance photocatalytic activity is increasingly common [15-20,21,22], however the actual function of the junction is rarely proven and correlated to catalytic activity. Here, TA measurements demonstrate that the presence of the ZnO/$CuWO_4$ junction greatly increases the electron-hole lifetimes of the photocatalysts and this is proposed to be the dominant factor behind the increased level of photocatalytic activity. It is striking that the ZnO/$CuWO_4$ material exhibits extremely long photogenerated charge lifetimes exceeding many of those previously reported in the literature [21,36-38]. Although $CuWO_4$ has suitable band energetics to make it a suitable photocatalyst itself we found, in line with past studies [60], that very fast electron-hole recombination occurs following excitation of $CuWO_4$ charge nanoparticles, limiting its activity. $CuWO_4$ is however demonstrated to be an effective acceptor of ZnO photoelectrons, and critically these transferred photoelectrons are found to be still be accessible and suitably energetic to participate in environmental remediation reactions via oxygen reduction. This demonstrates an alternative application for $CuWO_4$ as a sensitized electron acceptor and future work will explore the potential use of visible light absorbing materials to couple to $CuWO_4$ to extend activity into the visible region.

Acknowledgements

This work was supported by European Commission under grant FP7 Marie Curie Career Integration Grant (HETMAT, Project No. 322114). The research is also financed in part by Slovenian Research Agency Programs No. P2-0377. T. Mavrič gratefully acknowledges the Slovenian Research Agency for funding of the Ph.D. scholarship. A.J. Cowan gratefully acknowledges a fellowship from the EPSRC (EP/K006851/1) and M. Forster acknowledges the EPRSC for funding of the studentship. T. Mavrič would like to thank Mojca Žorž and Petra Makorič for their assistance with HPLC measurements.

Appendix A. Supplementary data

Supplementary data associated with this article can be found, in the online version, at doi:XXXX.

References

[1] D. Ravelli, D. Dondi, M. Fagnoni, A. Albini, Photocatalysis. A multi-faceted concept for green chemistry, Chem. Soc. Rev. 38 (2009) 1999−2011.
[2] C. Yu, W. Zhou, H. Liu, Y. Liu, D.D. Dionysiou, Design and fabrication of microsphere photocatalysts for environmental purification and energy conversion, Chem. Eng. J. 287 (2016) 117−129.
[3] E. Pelizzetti, V. Maurino, C. Minero, V. Carlin, M.L. Tosato, E. Pramauro, O. Zerbinati, Photocatalytic degradation of atrazine and other s-triazine herbicides, Environ. Sci. Technol. 24 (1990) 1559−1565.
[4] M.M. Gao, L.L. Zhu, W.L. Ong, J. Wang, G.W. Ho, Structural design of TiO_2-based photocatalyst for H_2 production and degradation applications, Catal. Sci. Technol. 5 (2015) 4703−4726.
[5] K.M. Lee, C.W. Lai, K.S.Ngai, J.C. Juan, Recent developments of zinc oxide based photocatalyst in water treatment technology: A review, Water. Res. 88 (2016) 428−448.
[6] A. Janotti, C.G. Van de Walle, Fundamentals of zinc oxide as a Semiconductor, Rep. Prog. Phys. 72 (2009) 126501.
[7] S.G. Kumar, K.S.R.K. Rao, Zinc oxide based photocatalysis: tailoring surface-bulk structure and related interfacial charge carrier dynamics for better environmental applications, RSC Adv. 5 (2015) 3306−3351.
[8] H. Tong, S.X. Ouyang, Y.P. Bi, N. Umezawa, M. Oshikiri, J.H. Ye, Nano-photocatalytic materials: possibilities and challenges, Adv. Mater. 24 (2012) 229−251.
[9] R. Marschall, L.Z. Wang, Non-metal doping of transition metal oxides for visible-lightphotocatalysis, Catal. Today 225 (2014) 111−135.
[10] Y.J. Cho, H.I. Kim, S. Lee, W. Choi, Dual-functional photocatalysis using a ternary hybrid of TiO_2 modified with graphene oxide along with Pt and fluoride for H_2-producing water treatment, J. Catal. 330 (2015) 387−395.

[11] D. Su, J.Y. Wang, Y.P. Tang, C. Liu, L.F. Liu, X.J. Han, Constructing WO_3/TiO_2 composite structure towards sufficient use of solar energy, Chem. Commun. 47 (2011) 4231−4233.
[12] D. Yang, Y.Y. Sun, Z.W. Tong, Y. Tian, Y.B. Li, Z.Y. Jiang, Synthesis of Ag/TiO_2 nanotube heterojunction with improved visible-light photocatalytic performance inspired by bioadhesion, J. Phys. Chem. C 119 (2015) 5827−5835.
[13] V. Stengl, D. Popelkova, P. Vlacil, TiO_2-graphene nanocomposite as high performace photocatalysts, J. Phys. Chem. C 115 (2011) 25209−25218.
[14] H.L. Wang, L.S. Zhang, Z.G. Chen, J.Q. Hu, S.J. Li, Z.H. Wang, J.S. Liu, X.C. Wang, Semiconductor heterojunction photocatalysts: design, construction, and photocatalytic performances, Chem. Soc. Rev. 43 (2014) 5234−5244.
[15] S. Balachandran, M. Swaminathan, Facile fabrication of heterostructured Bi_2O_3−ZnO photocatalyst and its enhanced photocatalytic activity, J. Phys. Chem. C 116 (2012) 26306−26312.
[16] H.R. Pant, C.H. Park, B. Pant, L.D. Tijing, H.Y. Kim, C.S. Kim, Synthesis, characterization, and photocatalytic properties of ZnO nano-flower containing TiO_2 NPs, Ceram. Int. 38 (2012) 2943−2950.
[17] A. Hamrouni, H. Lachheb, A. Houas, Synthesis, characterization and photocatalytic activity of ZnO-SnO_2 Nanocomposites, Mater Sci. Eng. B-Adv 178 (2013) 1371−1379.
[18] S. Adhikari, D. Sarkar, G. Madras, Highly efficient WO_3–ZnO mixed oxides for photocatalysis, RSC Adv. 5 (2015) 11895−11904.
[19] D. Barpuzary, Z. Khan, N. Vinothkumar, M. De, M. Qureshi, Hierarchically grown urchinlike CdS@ZnO and CdS@Al_2O_3 heteroarrays for efficient visible-light-driven photocatalytic hydrogen generation, J. Phys. Chem. C 116 (2012) 150−156.
[20] S. Cho, J.W. Jang, J.S. Lee, K.H. Lee, Porous ZnO–ZnSe nanocomposites for visible light photocatalysis, Nanoscale 4 (2012) 2066−2071.
[21] X.Q. Xiong, H.H. Chen, Y.M. Xu, Improved photocatalytic activity of TiO_2 on the addition of $CuWO_4$, J. Phys. Chem. C 119 (2015) 5946−5953.
[22] J. Jiang, X. Zhang, P. Sun, L. Zhang, ZnO/BiOI heterostructures: photoinduced charge-transfer property and enhanced visible-light photocatalytic activity, J. Phys. Chem. C 115 (2011) 20555−20564.
[23] C. Zhang, J. Zhang, Y. Su, M. Xu, Z. Yang, Y. Zhang, ZnO nanowire/reduced graphene oxide nanocomposites for significantly enhanced photocatalytic degradation of Rhodamine 6G, Physica E 56 (2014) 251−255.
[24] V. Kuzhalosai, B. Subash, A. Senthilraja, P. Dhatshanamurthi, M. Shanthi, Synthesis, characterization and photocatalytic properties of SnO_2–ZnO composite under UV-A light, Spectrochim. Acta Mol. Biomol. Spectrosc. 115 (2013) 876−882.
[25] W. Liao, T. Zheng, P. Wang, S. Tu, W. Pan, Efficient microwave-assisted photocatalytic degradation of endocrine disruptor dimethyl phthalate over composite catalyst ZrO_x/ZnO, J. Environ. Sci. 22 (11) (2010) 1800−1806.
[26] S.-M. Lam, J.-C. Sin, I. Satoshi, A.Z. Abdullah, A.R. Mohamed, Enhanced sunlight photocatalytic performance over Nb_2O_5/ZnOnanorod composites and the mechanism study, Appl. Catal. A-Gen 471 (2014) 126−135.
[27] M. Valenti, D. Dolat, G. Biskos, A. Schmidt-Ott, W.A. Smith, Enhancement of the photoelectrochemical performance of $CuWO_4$ thin films for solar water splitting by plasmonic nanoparticle functionalization, J. Phys. Chem. C 119 (2015) 2096−2104.
[28] N. Gaillard, Y. Chang, A. DeAngelis, S. Higgins, A. Braun, A nanocomposite photoelectrode made of 2.2 eV band gap copper tungstate ($CuWO_4$) and multi-wall carbon nanotubes for solar-assisted water splitting, Int. J. Hydrogen Energy 38 (2013) 3166−3176.
[29] H. Chen, W. Leng, Y. Xu, Enhanced visible-light photoactivity of $CuWO_4$ through a Surface-deposited CuO, J. Phys. Chem. C 118 (2014) 9982−9989.
[30] K. Vignesh, R. Priyanka, R. Hariharan, M. Rajarajan, A. Suganthi, Fabrication of CdS and $CuWO_4$ modified TiO_2 nanoparticles and its photocatalytic activity under visible light irradiation, J. Ind. Eng. Chem. 20 (2014) 435−443.
[31] T. Montini, V. Gombac, A. Hameed, L. Felisari, G. Adami, P. Fornasiero, Synthesis, characterization and photocatalytic performance of transition metal tungstates, Chem. Phys. Lett. 498 (2010) 113−119.
[32] U.M. García-Pérez, A. Martínez-de la Cruz, J. Peral, Transition metal tungstates synthesized by co-precipitation method: Basic photocatalytic properties, Electrochim. Acta 81 (2012) 227−232.
[33] J.C. Hill, K.S. Choi, Synthesis and characterization of high surface area $CuWO_4$ and Bi_2WO_6 electrodes for use as photoanodes for solar water oxidation, J. Mater. Chem. A 1 (2013) 5006−5014.
[34] H. Zhang, P. Yilmaz, J.O. Ansari, F.F. Khan, R. Binions, S. Krause, S. Dunn, Incorporation of Ag nanowires in $CuWO_4$ for improved visible light-induced photoanode performance, J. Mater. Chem. A 3 (2015) 9638−9644.
[35] A. Thomas, C. Janaky, G.F. Samu, M.N. Huda, P. Sarker, J.P. Liu, V. van Nguyen, E.H. Wang, K.A. Schug, K. Rajeshwar, Time- and energy-efficient solution combustion synthesis of binary metal tungstate nanoparticles with enhanced photocatalytic activity, ChemSusChem 8 (2015) 1652−1663.
[36] I. Robel, V. Subramanian, M. Kuno, P.V. Kamat, Quantum dot solar cells. Harvesting light energy with CdSe nanocrystals molecularly linked to mesoscopic TiO2 films, J. Am. Chem. Soc. 128 (2006) 2385–2393.

[37] I. Grigioni, K.G. Stamplecoskie, E. Selli, P.V. Kamat, Dynamics of photogenerated charge carriers in $WO_3/BiVO_4$ heterojunction photoanodes, J. Phys. Chem. C 119 (2015) 20792-20800.
[38] P.K. Santra, P.V. Nair, K.G. Thomas, P.V. Kamat, $CuInS_2$-Sensitized quantum dot solar cell. Electrophoretic deposition, excited-state dynamics, and photovoltaic performance, J. Phys. Chem. Lett. 4 (2013) 722-729.
[39] T. Mavrič, S. Emin, M. Valant, W. Peng, U.L. Stangar, The role of polyvinylpyrrolidone in hydrothermally synthesized Ag/ZnO nanocomposites and their photocatalytic activities, J. Nanosci. Nanotechnol. 15 (2015) 6541−6549.
[40] A.E. Morales, E.S. Mora, U. Pal, Use of diffuse reflectance spectroscopy for optical characterization of un-supported nanostructures, Rev. Mex. Fis. S 53 (2007) 18−22.
[41] S. Emin, D. Lisjak, M. Pitcher, M. Valant, Structural and morphological transformations of textural porous zinc sulfide microspheres, Micropor. Mesopor. Mat. 165 (2013) 185−192.
[42] J.E. Yourey, J.B. Kurtz, B.M. Barlett, Water Oxidation on a $CuWO_4$−WO_3 Composite Electrode in the Presence of $[Fe(CN)_6]^{3-}$: Toward Solar Z-Scheme Water Splitting at Zero Bias, J. Phys. Chem. C 116 (2012) 3200−3205.
[43] S. Dey, R.A. Ricciardo, H.L. Cuthbert, P.M. Woodward, Metal-to-Metal Charge Transfer in AWO_4 (A = Mg, Mn, Co, Ni, Cu, or Zn) Compounds with the Wolframite Structure, Inorg. Chem. 53 (2014) 4394−4399.
[44] S. Emin, M. Fanetti, F.F. Abdi, D. Lisjak, M. Valant, R. van de Krol, B. Dam, Photoelectrochemical properties of cadmium chalcogenide-sensitized textured porous zinc oxide plate electrodes, ACS Appl. Mater. Interfaces 5 (2013) 1113−1121.
[45] H. Chen, Y. Xu, Photocatalytic organic degradation over W-rich and Cu-rich $CuWO_4$ under UV and visible light, RSC Adv. 5 (2015) 8108−8113.
[46] Z.G. Jia, K.K. Peng, Y.H. Li, R.S. Zhu, Preparation and photocatalytic performance of porous ZnO microrods loaded with Ag, T. Nonferr. Metal. Soc. 22 (2012) 873−878.
[47] S.J. Naik, A.V. Salker, Solid state studies on cobalt and copper tungstates nano materials, Solid State Sci. 12 (2010) 2065−2072.
[48] J.K. Cooper, Y. Ling, C. Longo, Y. Li, J.Z. Zhang, Effects of hydrogen treatment and air annealing on ultrafast charge carrier dynamics in ZnO nanowires under in situ photoelectrochemical conditions, J. Phys. Chem. C 116 (2012) 17360−17368.
[49] B. Enright, D. Fitzmaurice, Spectroscopic determination of electron and hole effective masses in a nanocrystalline Semiconductor Film, J. Phys. Chem. 100 (1996) 1027−1035.
[50] C. Bauer, G. Boschloo, E. Mukhtar, and A. Hagfeldt, Ultrafast relaxation dynamics of charge carriers in ZnO nanocrystalline thin films, Chem. Phys. Lett. 387 (2004) 176–181.
[51] M. Li, G. Xing, G. Xing, B. Wu, T. Wu, X. Zhang, and T. C. Sum, Origin of green emission and charge trapping dynamics in ZnO nanowires, Phys. Rev. B 87 (2013) 1–8.
[52] A. Nageswara Rao, B. Sivasankar, V. Sadasivam, Kinetic studies on the photocatalytic degradation of Direct Yellow 12 in the presence of ZnO catalyst, J. Mol. Catal. Chem. 306 (2009) 77−81.
[53] B. Ikizler, S. Peker, Stability of ZnO nanorods coated on the channel wall under continuous flow conditions, Adv. Mat. Lett. 5(6) (2014) 325−332.
[54] X.H. Lin, S.N. Lee, W. Zhang, S.F.Y. Li, Photocatalytic degradation of terephthalic acid on sulfated titania particles and identification of fluorescent intermediates, J. Hazard. Mater. 303 (2016) 64−75.
[55] Y. Zhang, Z. Cai, X. Ma, Photocatalysis enhancement of Au/BFO nanoparticles using plasmon resonance of AuNPs, Physica B 479 (2015) 101−106.
[56] U. Černigoj, M. Kete, U.L. Štangar, Development of a fluorescence-based method for evaluation of self-cleaning properties of photocatalytic layers, Catal. Today 151 (2010) 46−52.
[57] A. Shafaei, M. Nikazar, M. Arami, Photocatalytic degradation of terephthalic acid using titania and zinc oxide photocatalysts: Comparative study, Desalination 252 (2010) 8−16.
[58] K. Bubacz, E. Kusiak-Nejman, B. Tryba, A.W. Morawski, Investigation of OH radicals formation on the surface of TiO_2/N photocatalyst at the presence of terephthalic acid solution. Estimation of optimal conditions, J. Photochem. Photobiol. A 261 (2013) 7−11.
[59] K. Ishibashi, A. Fujishima, T. Watanabe, K. Hashimoto, Detection of active oxidative species in $Ti0_2$ photocatalysis using the fluorescence technique, Electrochem. Commun. 2 (2000) 207−210.
[60] K.J. Pyper, J.E. Yourey, B.M. Bartlett, Reactivity of $CuWO_4$ in photoelectrochemical water oxidation is dictated by a midgap electronic state, J. Phys. Chem. C 117 (2013) 24726−24732.

Figures

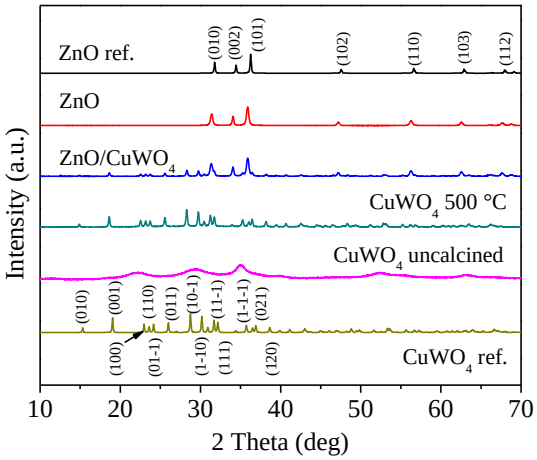

Fig.1. (a) XRD patterns of ZnO, $CuWO_4$ (uncalcined), $CuWO_4$ (calcined at 500 °C) and ZnO/$CuWO_4$ powder samples. The reference patterns of ZnO (above) and $CuWO_4$ (below) are taken from the COD database.

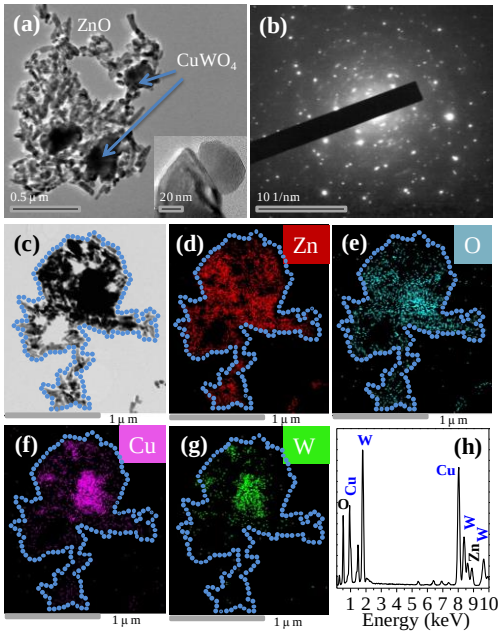

Fig. 2. (a) TEM image of the ZnO/$CuWO_4$ NC obtained by mixing and drying (100 °C) of individual ZnO and $CuWO_4$ NPs. (b) Shows recorded SAED pattern of ZnO /$CuWO_4$ NC taken from (a). STEM image (c) and elemental maps (d-g) of ZnO/$CuWO_4$ NC together with the corresponding EDX spectrum (h).

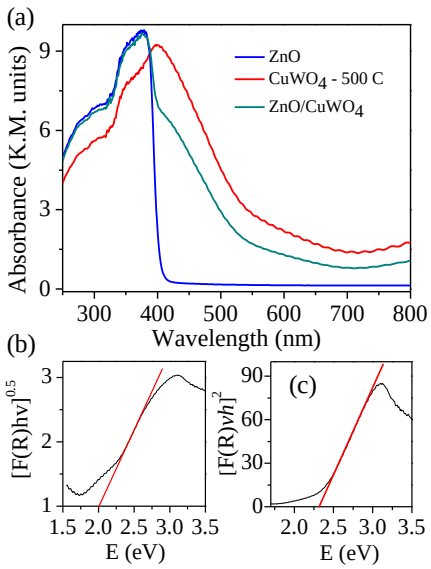

Fig. 3. (a) Absorption spectra of ZnO, $CuWO_4$, (calcined at 500 °C), and ZnO/$CuWO_4$. In (b) is given the indirect and in (c) the direct band gaps of $CuWO_4$ (500 °C) sample.

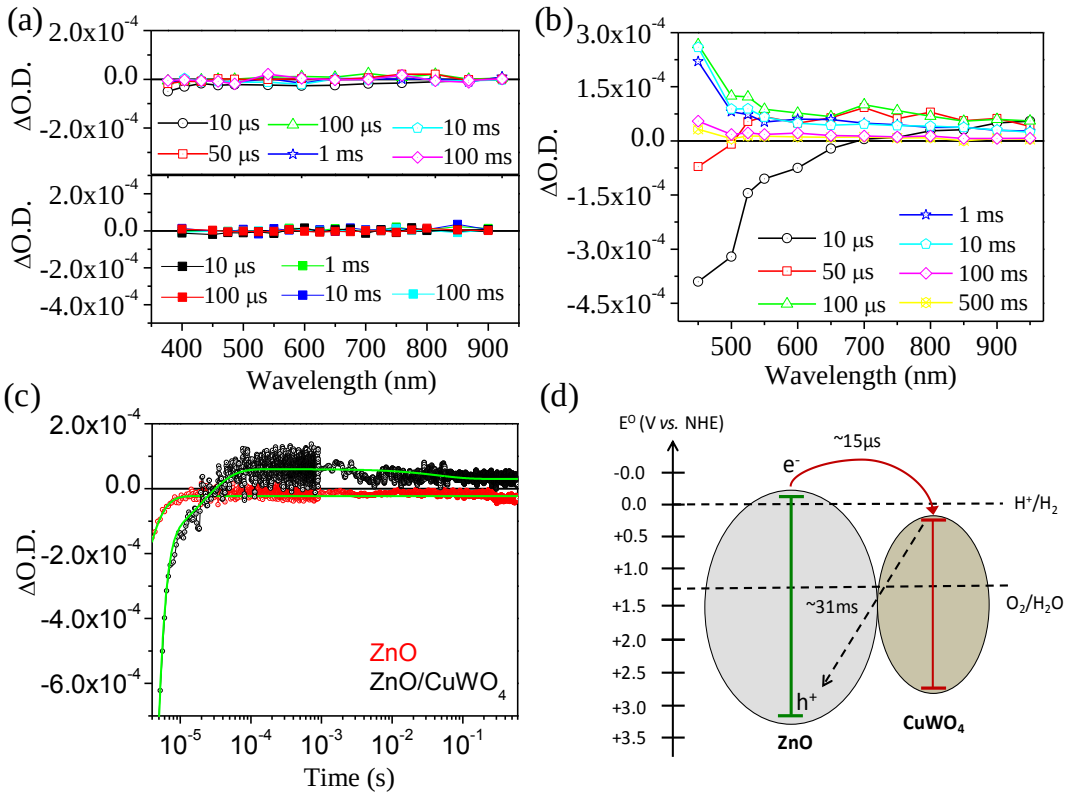

Fig. 4. TA spectrum recorded following UV (355 nm) excitation of (a) ZnO (upper) and $CuWO_4$ (lower) and (b) ZnO/$CuWO_4$ NC under an Ar environment. (c) TA kinetics following of ZnO and ZnO/$CuWO_4$ UV upon excitation (355 nm) under an Ar environment recorded at 550 nm. In (d) is shown a proposed mechanism of photoinduced electron transfer between phases in ZnO/$CuWO_4$ NC, with the direction of electron transfer indicated by the arrows.

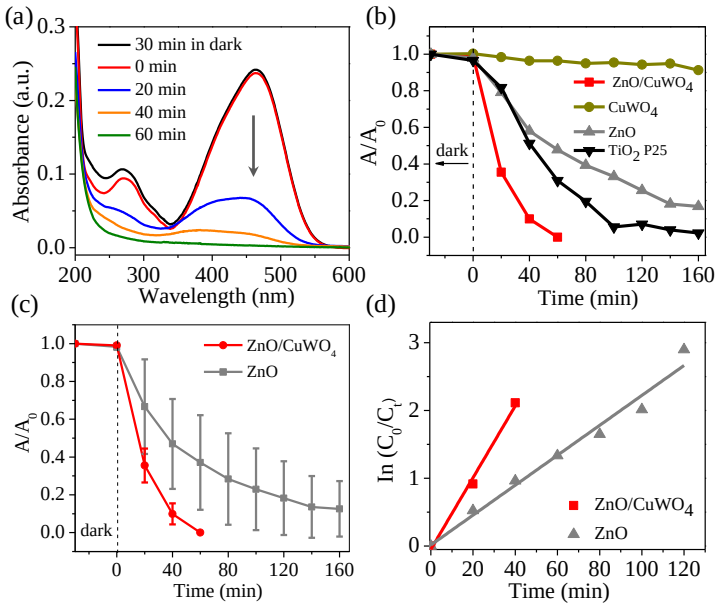

Fig. 5. (a) UV-vis absorption spectra of MO taken before and after the photocatalytic tests. (b) Photocatalytic decolorization of 1×10^{-5} M MO in the presence of different photocatalytic powders under UV-Vis light. (c) Error bars obtained from 3 experiments. (d) First order kinetics plots for ZnO and $ZnO/CuWO_4$ samples.

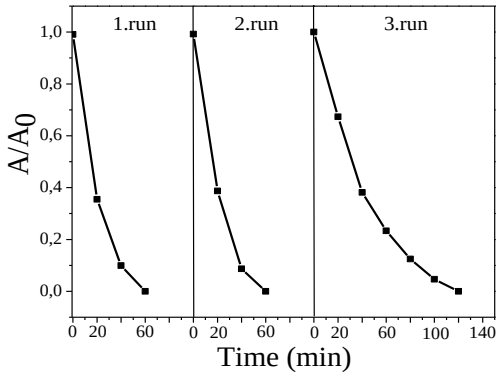

Fig. 6. Reusability efficiency of the $ZnO/CuWO_4$ for decolourization of 1×10^{-5} M MO.

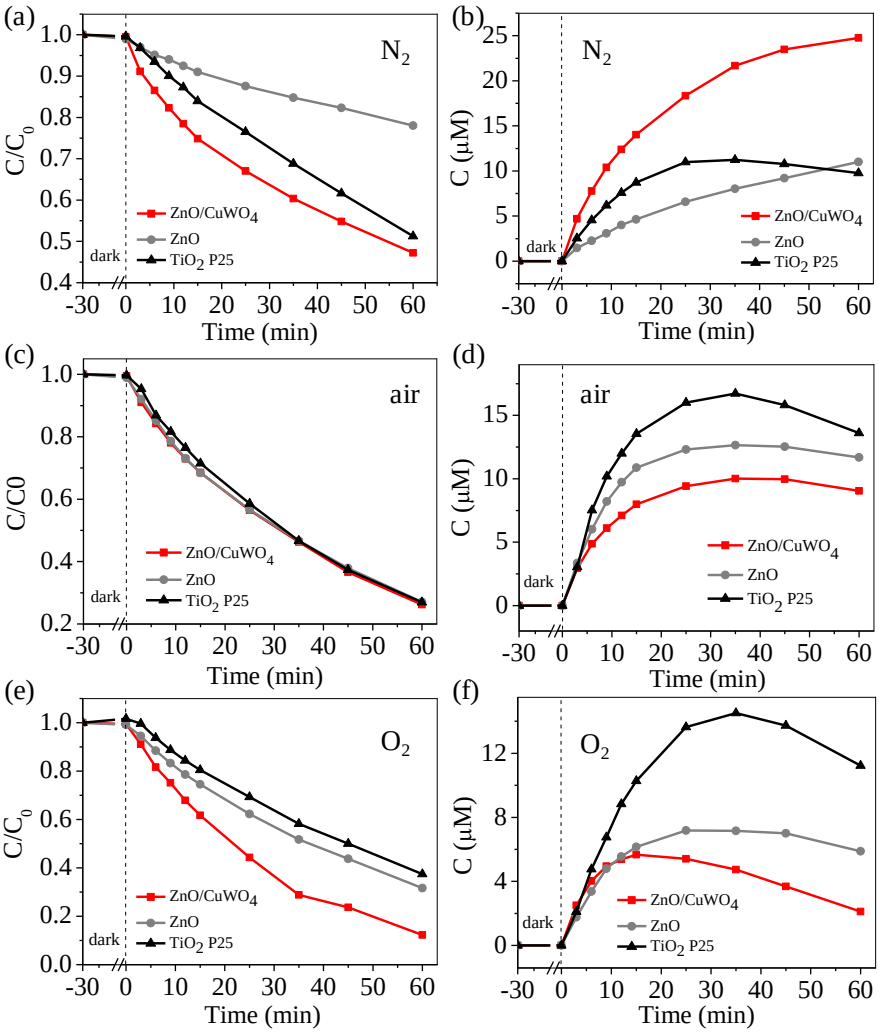

Fig. 7. Noramlized photocatalytic efficiency of ZnO, $CuWO_4$, TiO_2-P25, and ZnO/$CuWO_4$ NPs for degradation of 1×10^{-4} M TPA under (a) N_2, (c) air and (e) O_2 detected with HPLC. Time dependent change of HTPA concentration during the photocatalytic degradation under (b) N_2, (d) air and (f) O_2.

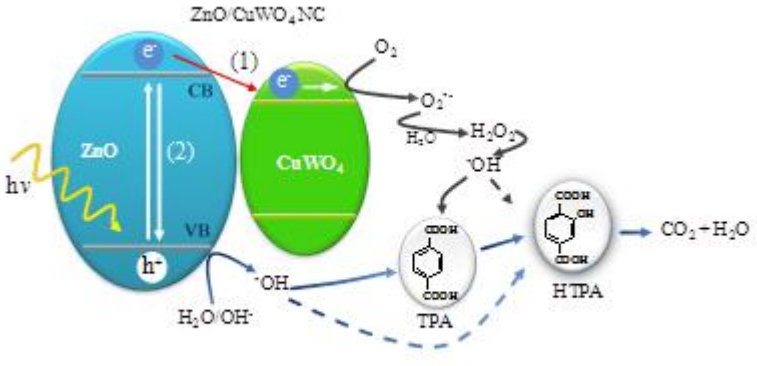

Fig. 8. Scheme of photocatalytic degradation of TPA in the presence of ZnO/$CuWO_4$ NC. Arrows show the reaction paths of photoexcited electrons in ZnO with (1) showing transfer to $CuWO_4$ phase and (2) recombinations with holes inside ZnO.